



Selective cellobiose photoreforming for simultaneous gluconic acid and syngas production in acidic conditions

Jiu Wang ^a, Heng Zhao ^{a,b}, Lin Chen ^{c,*}, Jonas Björk ^c, Johanna Rosen ^c, Pawan Kumar ^a, Liquan Jing ^a, Jun Chen ^d, Md Golam Kibria ^{a,*}, Jinguang Hu ^{a,*}

^a Department of Chemical and Petroleum Engineering, University of Calgary, 2500 University Drive, NW, Calgary, Alberta T2N1N4, Canada

^b Eastern Institute for Advanced Study, Eastern Institute of Technology, Ningbo, Zhejiang 315200, China

^c Materials Design Division, Department of Physics, Chemistry and Biology, IFM, Linköping University, Linköping 58183, Sweden

^d State Key Laboratory of Advanced Technology for Materials Synthesis and Processing, Wuhan University of Technology, 122 Luoshi Road, Wuhan 430070, Hubei, China



ARTICLE INFO

Keywords:

Cellobiose photoreforming
Acidic conditions
Bifunctional photocatalyst
Gluconic acid
Syngas production

ABSTRACT

Here, we demonstrate the selective cellobiose (building block of cellulose) photoreforming for gluconic acid and syngas co-production in acidic conditions by rationally designing a bifunctional polymeric carbon nitride (CN) with potassium/sulfur co-dopant. This heteroatomic doped CN photocatalyst possesses enhanced visible light absorption, higher charge separation efficiency than pristine CN. Under acidic conditions, cellobiose is not only more efficiently hydrolyzed into glucose but also promotes the syngas and gluconic acid production. Density functional theory (DFT) calculations reveal the favorable generation of $\bullet\text{O}_2^-$ during the photocatalytic reaction, which is essential for gluconic acid production. Consequently, the fine-designed photocatalyst presents excellent cellobiose conversion (>80%) and gluconic acid selectivity (>70%) together with the co-production of syngas ($\sim 56 \mu\text{mol g}^{-1} \text{h}^{-1}$) under light illumination. The current work demonstrates the feasibility of biomass photoreforming with value-added chemicals and syngas co-production under mild condition.

1. Introduction

Biomass valorization into fuels and chemicals has consistently been regarded as one of most prospective approaches to alleviate the energy crisis and environmental issues [1,2]. Compared to the traditional platforms for biomass valorization such as thermal and biological treatment, photocatalysis holds prominent features in energy saving and environmental protection [3,4]. Cellulose is the most abundant biomass component, which puts forward to high demands on photocatalyst design and reaction system regulation to efficiently convert cellulose into value-added chemicals and fuels. Recent years, we and others have successfully converted cellulose chemical building block glucose into fructose, arabinose, gluconic acid and 5-hydroxymethylfurfural (HMF) via rational designed photocatalysis process [5–8]. Beyond the chemical building block glucose, the structure building block of cellulose is cellobiose, which is a dimer of glucose linked via β -1,4-glycosidic bond and is the repetitive unit of cellulose in nature [9]. Therefore, understanding the mechanism of cellobiose photocatalytic conversion is an essential next step for cellulose photoreforming. So far, there are only

few studied explored cellobiose photoreforming under neutral solution [10]. However, to the best of our knowledge, no study has investigated the cellobiose photocatalytic conversion under acidic conditions, which is a more favorable environment for β -1,4-glycosidic bonds cleavage [11,12].

Our previous investigation reveals the gluconic acid production from cellobiose photoreforming under neutral solution [10]. The reactive oxygen species such as $\bullet\text{O}_2^-$ and $\bullet\text{OH}$ play significant role in the cellobiose conversion. However, the cellobiose conversion and gluconic acid selectivity is extremely low due to the recalcitrant β -1,4-glycosidic bonds. Acidic condition not only benefits cellobiose hydrolytic conversion into glucose, but also is more kinetically prone to H_2 production [13]. In this case, reactive oxygen species can better convert glucose into gluconic acid rather than involving in the oxidative breaking of β -1,4-glycosidic bonds, which are primarily cleaved by acidic hydrolysis. Additionally, CO could be generated from the dehydration process of formic acid as a common by-product of photoreforming process. Therefore, we expect a better production of gluconic acid and syngas from cellobiose photoreforming under acidic conditions.

* Corresponding authors.

E-mail addresses: lin.chen@liu.se (L. Chen), md.kibria@ucalgary.ca (M.G. Kibria), jinguang.hu@ucalgary.ca (J. Hu).

To realize this concept, it is crucial to have a rational designed photocatalyst with bifunctionality. Polymeric carbon nitride (CN) is an auspicious photocatalyst due to its enduring physicochemical attributes, distinctive band position and advantageous response to visible light [14]. CN has been demonstrated in representative photocatalytic processes including H₂ evolution, CO₂ reduction, and biomass conversion into value-added products [15–18]. In addition, bifunctional CN has already been proven for simultaneous H₂ production and glucose isomerization into fructose [19]. However, pure CN still suffers low efficiency owing to the limited light absorption and severe recombination of charge carriers [20]. Elemental doping has been revealed to effectively modulate the electronic structure and extend the visible-light absorption of CN, thus leading to favorable photocatalytic efficiency for biomass conversion [19,21]. Therefore, we hypothesize that rational modification of CN via specific heteroatomic doping would lead to gluconic acid production coupled with syngas production in acidic conditions from cellobiose photoreforming.

In this study, we present the pioneering evidence of the feasibility of selective cellobiose photoreforming into gluconic acid along with syngas co-production in acidic conditions. The procedure is achieved via a finely design of CN photocatalyst with potassium/sulfur co-dopant, which imparts excellent visible light response and improved charge separation efficiency. Under acidic conditions, not only is cellobiose more efficiently hydrolyzed into glucose, but it also promotes the production of syngas and gluconic acid. Moreover, the exceptional performance of the modified CN, achieved through heteroatomic doping, enables the selective production of gluconic acid by generating •O₂[−], which is revealed by DFT calculations. Consequently, the fine designed photocatalyst exhibited > 80% cellobiose conversion and > 70% gluconic acid selectivity coupled with syngas production (~56 μmol g^{−1} h^{−1}). This work provides an alternative strategy for cellobiose photoreforming into gluconic acid and syngas under acidic conditions by rational design of bifunctional photocatalyst.

2. Experimental

2.1. Synthesis of the photocatalysts

CNKS-OH was synthesized as follows: 1 g melamine and 0.5 g thiourea together with 7.5 g potassium chloride and 200 mg sodium hydroxide were meticulously and the mixture was heated in a crucible at a heating rate of 10 °C per minute, reaching a temperature of 520 °C, and maintained under an air atmosphere for 4 h. The obtained powders were then gently grounded and sonicated for 3 h in deionized water. To remove the soluble substance from the powder, it was completely washed, centrifuged for several times, and followed by drying at 70 °C overnight. Eventually, the resultant sample was marked as CNKS-OH.

For comparison, CNKS was obtained by the same method without the addition of sodium hydroxide, while MCN was synthesized adopting pure melamine under the identical reaction conditions.

2.2. Characterization

The XRD patterns had been recorded by Bruker D8 Advance. The FTIR spectra had been measured with a Nicolet iS 50 FTIR spectrometer. The UV-visible DRS had been obtained using a Lambda spectrometer (PerkinElmer). An F-4700 spectrophotometer and an FLS920 spectrophotometer had been used to measure the PL and TRPL spectra. XPS analysis was conducted by Escalab 250Xi, and 284.8 eV for adventitious C is used for calibration. The NMR spectra had been acquired by Bruker AVANCETM 600 MHz. HITACHI (SU8100) and Talos 200 had been used to collect FESEM and HRTEM. The ESR spectra had been recorded with the JES-X320 spectrometer (JEOL). The ESR experiments for detecting DMPO-•O₂[−] were carried out in methanol solution, while the detection

for DMPO-•OH was performed in an aqueous solution. Electrochemical tests were conducted using a CHI660D workstation. The working electrode was the FTO glass loaded with the sample, the counter electrode was made of platinum, and the reference electrode used was Ag/AgCl. 0.1 M Na₂SO₄ aqueous solution was used as the electrolyte. Vario EL Cube (Germany) had been used to measure the elemental analysis.

2.3. Photocatalytic measurements

For glucose photoreforming, photocatalytic tests were conducted using a 20 mL glass vial. A 10 mL glucose solution of 2 g/L was obtained, then 10 mg of catalyst was evenly distributed within it. The airtight reactor was placed in darkness and stirred for one hour, after which the photocatalytic reactions were initiated by a Xenon lamp with a power of 300 W. As for cellobiose photoreforming, 20 mg catalyst was evenly dispersed inside the cellobiose solution with 2 g/L concentration in the volume of 10 mL 0.1 M H₂SO₄. The photocatalytic reactions were kept the same as above procedures. The reaction temperature was measured to be 90 °C. The glucose, cellobiose and other products had been analysed via a refractive index detector (RID) along with a high-performance liquid chromatography (HPLC, 1200 Agilent) column and an Aminex HPX-87 H column (300 × 7.8 mm, Bio-Rad). The mobile phase was sulfuric acid at 0.6 mL/min flow rate with a concentration of 5 mM. The gluconic acid concentration can be further determined using high-performance liquid chromatography (Dionex ICS-6000) with a diode array detector (DAD) and an EclipseXDB-C18 column (4.6 × 250 mm, Agilent). Three repeated experiments were performed to obtain the error bars, and the corresponding calculations for glucose conversion, cellobiose conversion, gluconic acid selectivity/yield are presented below:

$$\text{Glucose conversion} = \frac{[\text{glucose}]_0 - [\text{glucose}]_T}{[\text{glucose}]_0} \times 100\%$$

$$\text{Cellobiose conversion} = \frac{[\text{cellobiose}]_0 - [\text{cellobiose}]_T}{[\text{cellobiose}]_0} \times 100\%$$

$$\text{Gluconic acid selectivity} = \frac{[\text{gluconic acid}]_T}{[\text{glucose}]_0 - [\text{glucose}]_T} \times 100\% \text{ or } \frac{[\text{gluconic acid}]_T}{[\text{cellobiose}]_0 - [\text{cellobiose}]_T} \times \frac{1}{2} \times 100\%$$

$$\text{Gluconic acid yield} = \frac{[\text{gluconic acid}]_T}{[\text{glucose}]_0} \times 100\% \text{ or } \frac{[\text{gluconic acid}]_T}{[\text{cellobiose}]_0} \times \frac{1}{2} \times 100\%$$

Subscript O and T refers to the molar concentration of the initial solution and of substance at T time, respectively.

2.4. Computational details

Density functional theory (DFT) calculations are conducted by the Vienna Ab-initio Simulation Package (VASP) [22–24]. In this method, the Kohn-Sham orbitals are represented using plane waves with an energy cut-off of 450 eV, and the interaction between the valence electrons and the cores is described using the plane augmented wave (PAW) approach [25,26]. The exchange-correlation effects are described within rev-vdW-DF2 functional [27], which includes van der Waals interactions and is known to be suitable for the layered materials in predicting the geometric properties [28]. The calculations consider the following number of valence electrons: 7 (K), 6 (S), 6 (O), 5 (N), 4 (C), and 1 (H). Structures are optimized with the conjugate gradient method and geometries are considered to be converged when the largest force on each atom is lower than 0.02 eV/Å and the electronic energy difference for the electronic structure minimization is lower than 1×10^{-5} eV. The pressure for H₂ and O₂ is maintained at 1 bar and VESTA is used for charge density difference plot [29]. The Bader charges are computed utilizing the algorithm from G. Henkelman's group [30,31].

3. Results and discussion

3.1. Materials design and characterizations

The modified carbon nitride by the co-doping of potassium and sulfur is produced by synthesizing melamine and thiourea, with the incorporation of potassium chloride and sodium hydroxide by one-step thermal calcination process, which is labelled as CNKS-OH (Fig. 1a). The control photocatalysts are obtained via the same method and without the addition of sodium hydroxide (CNKS), and using pure melamine (MCN), respectively. As shown in Fig. 1b, CNKS-OH exhibits similar stacked-nanosheets morphology by FESEM compared with MCN and

CNKS (Fig. S1), which is further demonstrated by transmission electron microscopy (TEM) image (Fig. 1c). High angle annular dark field scanning transmission electron microscopy (HAADF-STEM) image shows that the elements C, N, K, and S are uniformly distributed in CNKS-OH according to the elemental mappings (Fig. 1d). The presence of carbon nitride is confirmed through X-ray diffraction (XRD) analysis. As shown in Fig. S2, The XRD signals of MCN located at 13° and 27° are attributed to the (100) and (002) planes, respectively, which are characteristic of typical CNs. Note that the (100) signal of CNKS and CNKS-OH almost disappear, which could be owing to the distortion of the in-plane conformation caused by the interaction of potassium [32,33]. The appearance of the peak at 8° of CNKS-OH reveals the alternation of

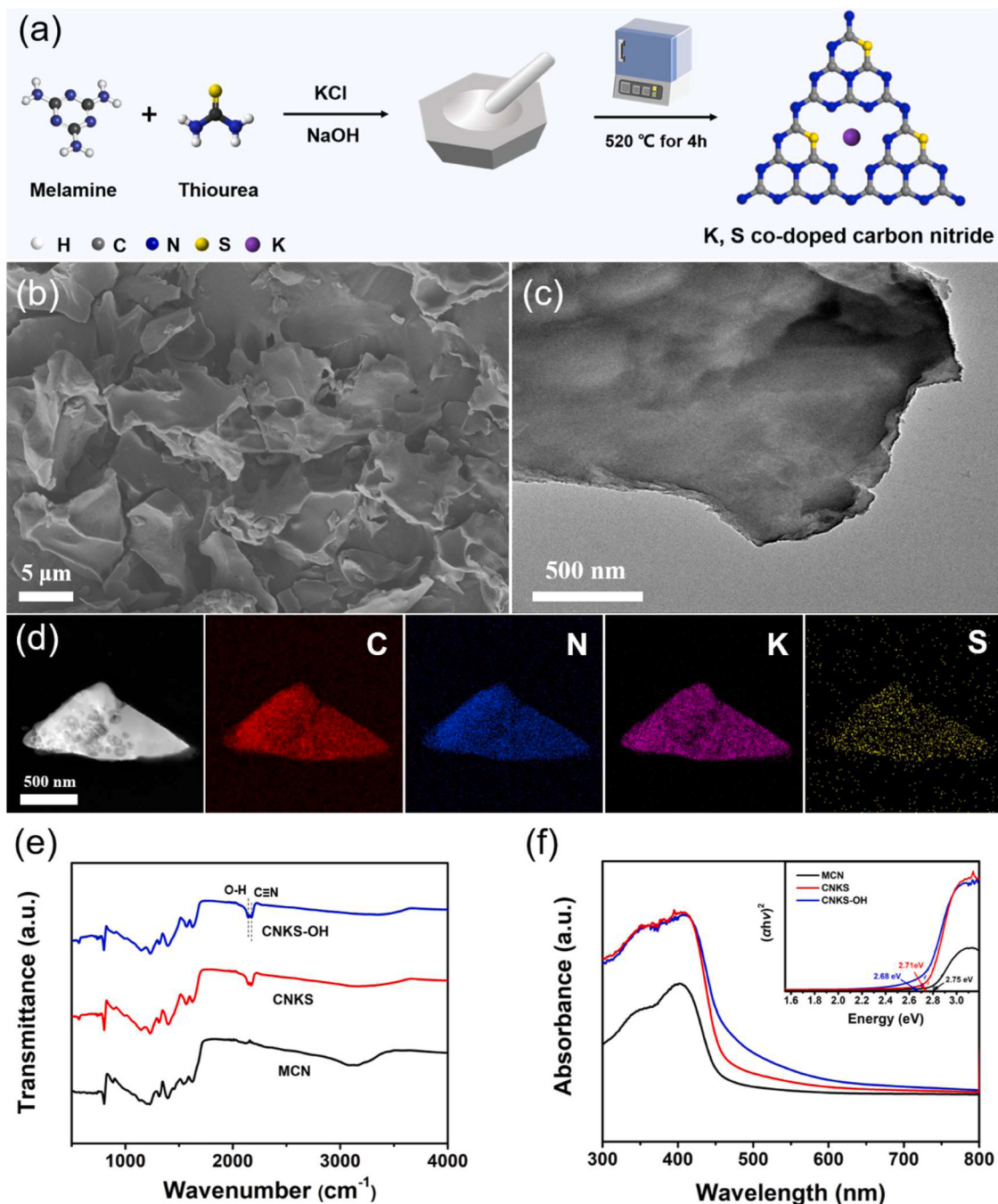


Fig. 1. (a) Synthetic process for K, S co-doped CN through one-step thermal copolymerization. (b) FESEM image, (c) TEM image and (d) HAADF-STEM image of CNKS-OH and corresponding elemental mappings of C, N, K, S. The colors of red, blue, purple, and yellow represent the elemental components of C, N, K, and S, respectively. (e) FTIR spectra and (f) UV-vis DRS of MCN, CNKS and CNKS-OH.

heptazine units of the in-plane structure by partially induced formation of triazine units [34]. In addition, the Fourier-transform infrared (FTIR) spectra are displayed in Fig. 1e. The signal observed at 810° can be attributed to the s-triazine rings, while the peaks between 1150 cm^{-1} and 1750 cm^{-1} indicate signals of C–N in heterocycles, providing further evidence of the formation of CN. The peaks observed at around 2150 cm^{-1} in CNKS and 2180 cm^{-1} in CNKS-OH can be attributed to the formation of terminal hydroxyl groups and cyano groups, respectively [35]. As shown in Fig. 1f, it should be noted that CNKS and CNKS-OH demonstrate noticeable red-shift and an improved absorption of visible light than that of MCN, revealing the alternation of electronic and optical properties by dopant arrangement within the CN structure [36]. Based on the Kubelka–Munk function, the band gaps of MCN, CNKS, and CNKS-OH are found to be 2.75 eV, 2.71 eV, and 2.68 eV, respectively (inset of Fig. 1f). The lower PL intensity of CNKS-OH suggests an improved charge separation compared with CNKS and MCN (Fig. S3).

X-ray photoelectron spectroscopy (XPS) is utilized to further investigate the elemental chemical states of the samples. As shown in Fig. 2a, MCN

The three peaks observed in the C 1 s spectrum at 284.8 eV, 286.6 eV (286.4 eV), and 288.2 eV correspond to adventitious carbon, C–NH₂, and N–C≡N within the heteroring [37]. It is worth noting that the peak signal of CNKS-OH around 286.6 eV is increased, providing additional evidence of cyano groups that share a similar binding energy with C–NH₂ groups [38]. Furthermore, the N 1 s spectra of MCN is divided into four peaks at 398.7, 399.4, 401.0, and 404.4 eV, which are associated with sp²-N, tertiary N, N within–NH₂ groups, and charging effects, respectively (Fig. 2b) [39–41]. The peaks of N 1 s corresponding to C–N = C and N–(C)₃ in CNKS-OH show a shift to lower binding energies, further revealing the existence of cyano groups and sulfur substitution on CNKS-OH [32,35]. As shown in Fig. S4a, the O 1 s peaks of CNKS-OH can be fitted into three peaks at 533.3, 532.0 and 531.4 eV, which are indicative of O–H, C–O and S–O, respectively [35]. The Cl 2p with 197.6 eV and 200.9 eV indicates the existence of chloride (Fig. S4b). Moreover, the K 2p orbitals are located at 292.9 eV and 295.7 eV, where the former could imply the formation of N–K (Fig. 2c) [42]. The K content of CNKS-OH is quantified for 6.1% through ICP study (Table S1). As

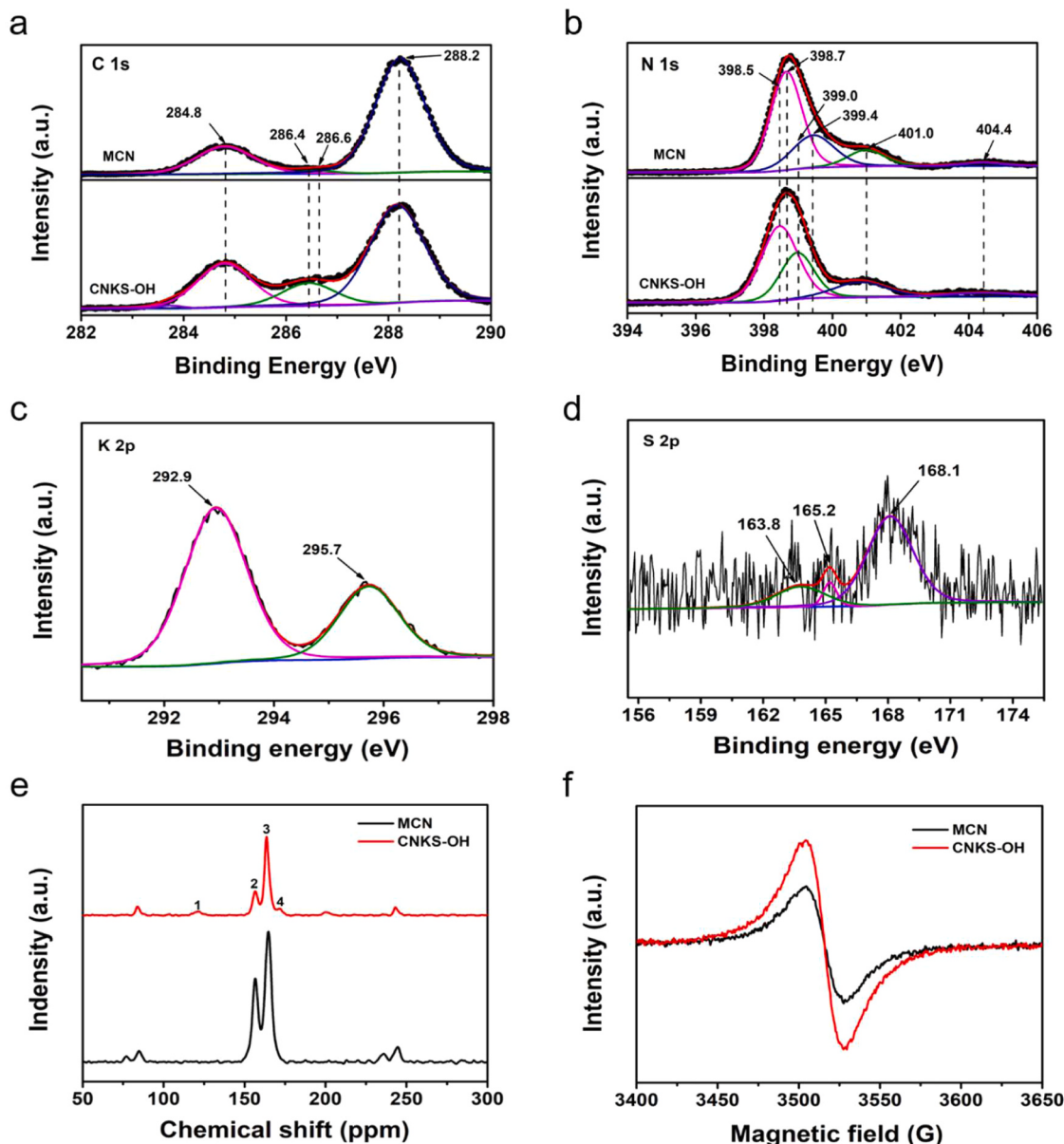


Fig. 2. High-resolution XPS spectra of (a) C 1 s and (b) N 1 s of MCN and CNKS-OH. High-resolution XPS spectra of (c) K 2p and (d) S 2p of CNKS-OH. (e) Solid-state ¹³C NMR spectra and (f) EPR spectra of MCN and CNKS-OH.

shown in Fig. 2d, it should be noted that S 2p orbitals can be assigned to N-S (165.2 eV), C-S (163.8 eV) and C-S-O (168.1 eV), respectively, demonstrating the self-doping of sulfur into the framework of CN with the introduction of thiourea [43]. The atomic configurations of MCN and CNKS-OH can be further clarified using solid-state ^{13}C NMR spectroscopy (Fig. 2e). The peaks observed in MCN at 156.5 ppm (C2) and 164.7 ppm (C3) are attributed to the CN_3 moiety and $\text{CN}_2\text{-}(\text{NH}_2)$ moiety, respectively. The result reveals that the heptazine core structure is not altered by alkali-assisted condensation process [44]. It should be noted that the peak intensities decreased obviously from MCN to CNKS-OH, indicating CNKS-OH has the lower condensation degree of melon units within CN structure. The two peaks at 121.2 ppm (C1) and 171.7 ppm (C4) are linked with carbon atoms of the cyano group and the adjacent carbon atoms connected to cyano groups, respectively [45]. The electronic properties of modified CN are further explored using electron paramagnetic resonance (EPR) spectra. As shown in Fig. 2f, CNKS-OH and MCN display a single Lorentzian line with a g-value of 2.0023 in their EPR spectra and the EPR signal of CNKS-OH is increased refer to MCN, which can be ascribed to heavier delocalization caused by heteroatomic doping [46].

3.2. Celloolose photoreforming

When the rationally designed photocatalyst is utilized for celloolose photoreforming, it indeed demonstrates great performance for gluconic acid and syngas production. As shown in Fig. 3a, CNKS-OH exhibits $> 90\%$ celloolose conversion within 6 h of reaction and corresponding glucose production increases with time, which is originated from the celloolose hydrolytic process in acidic solution. And CNKS-OH can undergo photocatalytic celloolose conversion under visible light irradiation (>400 nm) with $\sim 70\%$ conversion after 6-h and increasing glucose production as well (Fig. S5). Note that celloolose concentration decreases with reaction time, while glucose concentration keeps increasing

and exceeds the celloolose concentration at the half of the 6-h photocatalytic reaction (Fig. 3b). There is negligible gluconic acid production during the first 3-h reaction, indicating the celloolose hydrolysis is the dominant reaction during the first half of photoreforming process. However, it is interesting that when the glucose concentration exceeds celloolose concentration, glucose becomes the major substrate in the system where glucose photoreforming process into gluconic acid occurs at 3 h. In other words, the dominant reaction is hydrolytic process of celloolose at first half of the reaction and glucose photo-oxidation at second half of the reaction, respectively. As shown in Fig. 3c, $> 80\%$ celloolose conversion and $> 50\%$ gluconic acid yield can be achieved from glucose photo-oxidation process. Control experiment without light irradiation shows $\sim 45\%$ celloolose conversion and no gluconic acid production after 6-h reaction, suggesting the photogenerated radicals could play important roles in the gluconic acid production and the hydrolytic reaction of celloolose could be facilitated by in situ photocatalytic glucose conversion into gluconic acid. In addition, we conduct control experiment by controlling the circulation of condensate water, it exhibits little celloolose conversion ($< 10\%$) and negligible gluconic acid production after 6-h reaction (Fig. S6), revealing photothermal effects is essential for the selective celloolose conversion into gluconic acid. We later conduct the control experiments under water and alkaline solutions, while it exhibits negligible gluconic acid and H_2 production in neutral solution, suggesting few gluconic acid is produced from the celloolose oxidative cleavage. This is a hint that photogenerated reactive species could better convert glucose derived from celloolose hydrolysis into gluconic acid rather than involving in the oxidative breaking of $\beta\text{-}1,4$ -glycosidic bonds under acidic condition. Moreover, we conduct glucose photoreforming reaction under the same reaction conditions as celloolose photoreforming and it achieves $\sim 33\%$ glucose conversion and $\sim 60\%$ gluconic acid selectivity after 6-h reaction (Fig. S7). The results indicate gluconic acid can be obtained using glucose as substrate under acidic condition, which further reveals that gluconic acid is

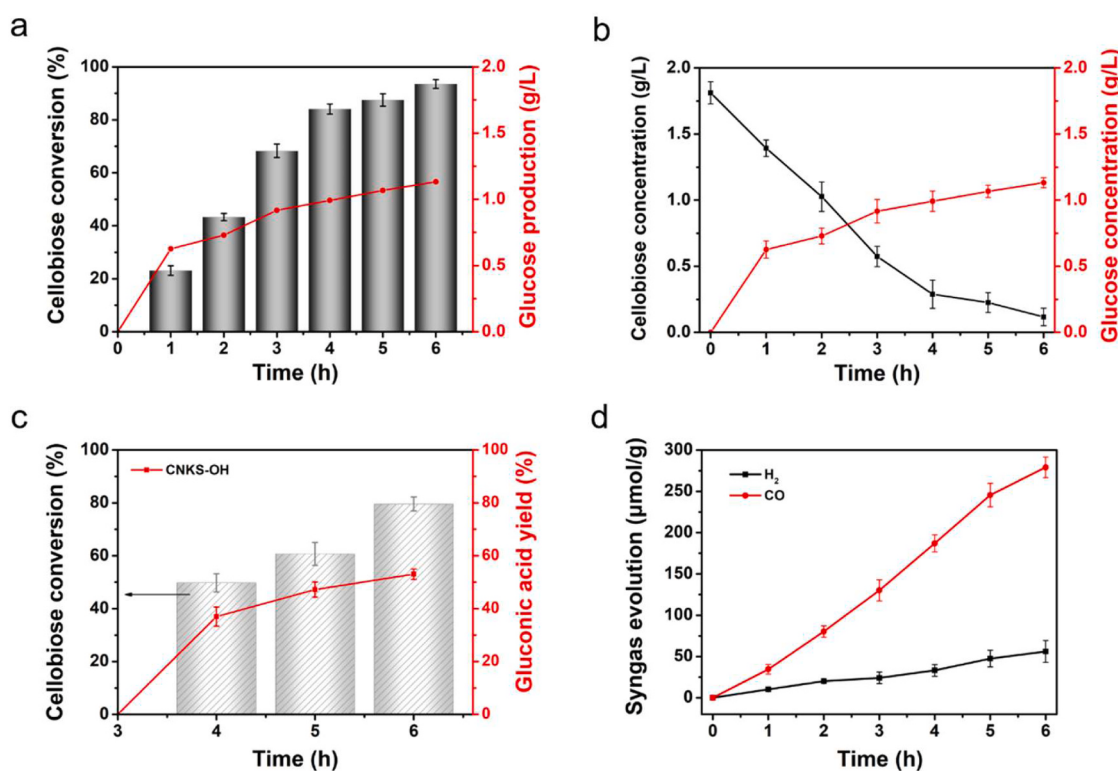


Fig. 3. (a) Celloolose conversion and glucose production of CNKS-OH upon 6-h photocatalytic reaction. (b) The corresponding celloolose concentration and glucose concentration over CNKS-OH upon 6-h irradiation. (c) Corresponding gluconic acid yield from glucose photo-oxidation process. (d) Simultaneous syngas production over CNKS-OH upon 6-h irradiation. Reaction conditions: 20 mg photocatalyst, 10 mL 2 g/L glucose solution in 0.1 M H_2SO_4 , 90 °C, air and 300 W Xenon lamp.

primarily produced by glucose derived from cellobiose acidic hydrolysis. Besides, other organic acid products such as lactic acid can be produced under alkaline solution, which is consistent with previous studies [17,18]. The results indicate that acidic condition is more favorable for cellobiose photoreforming process, which is beneficial for β -1,4-glycosidic bond cleavage from cellobiose into glucose and H_2 evolution. Apart from the liquid products from cellobiose photoreforming, the simultaneous generation of gaseous fuels would further facilitate cellobiose valorization. As such, syngas ($CO + H_2$) is simultaneously produced during the photoreforming process with CO/H_2 ratio of ~ 5 at the end of the reaction (Fig. 3d). Both CO and H_2 production are increasing with time, and reaches $\sim 280 \mu\text{mol/g}$ and $\sim 56 \mu\text{mol/g}$ upon 6-h irradiation, respectively. The H_2 is most likely generated from the reduction of protons in acidic solution by photogenerated electrons, while CO could be derived from the dehydration of formic acid during the photoreforming process [47].

In order to investigate the mechanism behind the cellobiose photoreforming into gluconic acid, glucose is selected as the initial substrate. It exhibits $\sim 60\%$ glucose conversion after 6-h reaction, while MCN and CNK obtain $\sim 33\%$ and negligible glucose conversion, respectively (Fig. 4a). The gluconic acid selectivity of the samples is decreasing, however, even after 6 h of reaction, CNKS-OH still retains $> 60\%$ gluconic acid selectivity (Fig. 4b). The calculated yield of gluconic acid at the conclusion of the photoreforming process is $\sim 35\%$ (Fig. 4c). Additionally, during the photoreforming process, additional products like

arabinose, glucaric acid and formic acid are detected (Fig. S8). These additional products might contribute to the decrease of gluconic acid selectivity, possibly due to the occurrence of over-oxidation process [48]. Hydrogen peroxide can be detected during the photocatalytic reaction (Fig. S9). The reaction pathway of H_2O_2 has been further demonstrated by rotating disk electrode (RDE) measurements to determine the average electron exchange number (n). As shown in Fig. S10, the linear sweep voltammetry (LSV) curve of CNKS-OH is measured on an RDE with different rotating speeds. The Koutecky-Levich plots are exhibited based on the current density value at -0.8 V versus $Ag/AgCl$ in the inset of Fig. S10, and the slope of linear regression determined the n value of CNKS-OH to be 2.010 ($R^2 = 0.9979$). The results indicate the electron transfer of CNKS-OH is more prone to $2e^-$ oxygen reduction for H_2O_2 production. In addition, we have quantified the production of H_2O_2 during the photocatalytic reaction (Fig. S11). It is found that the H_2O_2 concentration gradually decreases from $\sim 1930 \mu\text{M}$ to $\sim 590 \mu\text{M}$ until the end of 6-h photocatalytic reaction, most likely due to the exhaustion of oxygen in the reactor. The 18-hour cycling test shows outstanding recyclability of CNKS-OH (Fig. 4d). Additionally, we conduct stability test of CNKS-OH in cellobiose photoreforming under 18-h recyclable experiment, and it exhibits $\sim 80\%$ cellobiose conversion and $\sim 60\%$ gluconic acid selectivity after three cycles (Fig. S12), suggesting capable stability of CNKS-OH for cellobiose photoreforming. Scavenger experiments were then conducted to determine the main reactive species generated by CNKS-OH, which play significant roles in

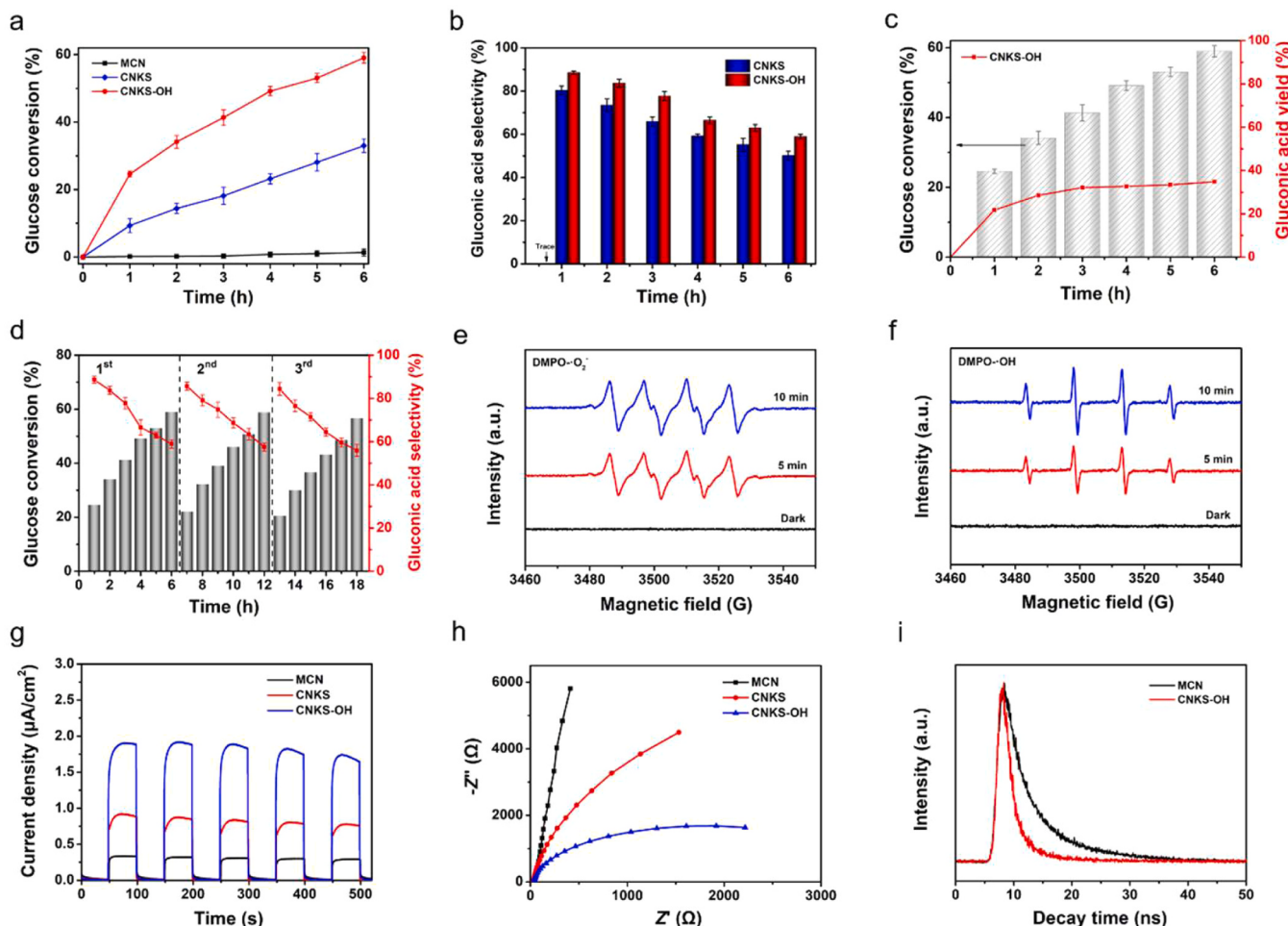


Fig. 4. (a) Glucose conversion and (b) corresponding gluconic acid selectivity of MCN, CNKS, and CNKS-OH upon 6-h irradiation. (c) Corresponding gluconic acid yield of CNKS-OH upon 6-h irradiation. (d) The recyclability of CNKS-OH for glucose photoreforming into gluconic acid during three cycles for 18 h. (e) ESR spectra of $DMPO\text{-}\bullet O_2$ and (f) $DMPO\text{-}\bullet OH$ for CNKS-OH in methanol dispersion and aqueous solution, respectively. (g) Transient photocurrent curves and (h) EIS Nyquist plots of the samples. (i) TRPL spectra of MCN and CNKS-OH. Reaction conditions: 10 mg photocatalyst, 10 mL 2 g/L glucose solution, air and 300 W Xenon lamp.

gluconic acid production during photoreforming process [6,49]. In these experiments, ethylenediaminetetraacetic acid disodium salt (EDTA-2Na), 1,4-benzoquinone (BQ), isopropanol (IPA) and sodium azide (NaN₃) were employed as scavengers of hole (h⁺), superoxide radical (•O₂⁻), hydroxyl radical (•OH) and singlet oxygen (¹O₂), respectively (Fig. S13). The addition of BQ, IPA, EDTA-2Na and NaN₃ resulted in a decrease in glucose conversion from 58.94% to 6.65%, 31.49%, 45.01%, and 54.65%, respectively, after a 6-hour reaction. The results demonstrate that the presence of •O₂⁻, •OH, h⁺ and ¹O₂ species is conducive to the photoreforming, while •O₂⁻ play the most important role, followed by •OH, in the photoreforming process to obtain gluconic acid. This is consistent with our previous investigation for the gluconic acid production from glucose photo-oxidation via a modified CN photocatalyst [49], during which favorable •O₂⁻ generation is the key for gluconic acid production. It is noted that •OH could have positive effect on deprotonation process of glucose for subsequent gluconic acid production [49,50]. In order to investigate the primary oxidative species involved during the photoreforming process of CNKS-OH, ESR spectra are obtained by utilizing 5,5-dimethyl-1-pyrroline N-oxide (DMPO) and 2,2,6,6-tetramethylpiperidine (TEMP) as spin trap. As illumination time increases, the characteristic peaks of •O₂⁻ signal intensify, indicating more •O₂⁻ are generated (Fig. 4e). In addition, the ESR spectra of DMPO-•O₂⁻ of MCN for comparison has also been conducted. As shown in Fig. S14, it exhibits negligible signal of •O₂⁻ after light illumination, suggesting the inferior performance of MCN in photo-generating •O₂⁻. As such, the DMPO-•OH signal cannot be observed under dark condition, but a rising signal can be seen under light irradiation (Fig. 4f), suggesting that more •OH are being generated with time. Additionally, the characteristic peaks of ¹O₂ signal become more pronounced with illumination time increases, revealing more ¹O₂ are involved in the reaction (Fig. S15). The experiments confirm the presence of •O₂⁻, •OH and ¹O₂ in the photoreforming process. To further identify the superior separation efficiency of CNKS-OH, we conducted transient photocurrent response spectra, electrochemical impedance spectra (EIS), and time-resolved photoluminescence (TRPL) spectra. The CNKS-OH exhibits the highest photocurrent intensity and smallest radius of the EIS Nyquist plots (Figs. 4g and 4h), revealing the better charge separation of CNKS-OH and its charge transfer resistance is lower. Besides, the average fluorescence lifetime of CNKS-OH reduces from 9.69 ns to 4.31 ns by comparison with MCN (Fig. 4i and Table S2), suggesting more effective photogenerated electrons migrate from bulk to the surface rather than recombination via nonradiative pathways, thus giving rise to improved charge separation efficiency [51,52]. The positive slopes observed in the Mott–Schottky plots indicate that both MCN and CNKS-OH can be classified as n-type semiconductors (Fig. S16a and S16b). The estimated positions of the conduction band are –0.78 eV and –0.95 eV [53]. Then, the band structures are provided in Fig. S16c and the generation of •O₂⁻ can be obtained via one-electron oxygen reduction reaction (1e-ORR) by photogenerated electrons in terms of thermodynamics [54]. These results indicate the modified carbon nitride shows superior photocatalytic efficiency and glucose can be served as an intermediate for gluconic acid production during the cellobiose photoreforming.

3.3. Theoretical calculations and mechanism investigation

Then density functional theory (DFT) calculations are performed to further understand the gluconic acid production of modified carbon nitride co-doped by K and S atoms. Model structure for heptazine-based carbon nitrides is considered as it is the most stable phase of CN at ambient conditions [55]. During geometry optimization, it was observed that the potassium ion shows a preference for intercalating the interlayer of CN and linking the layers by forming bonds with the nitride pores, which is similar to previous studies [33,56]. A 2 × 2 supercell of CN is constructed to study the reactions. The theoretical lattice constant of CN and K-doped CN is determined by Birch–Murnaghan equation of state (Fig. S17). Considering the low concentration of introduced sulfur

during the experiments, one nitrogen is replaced by one sulfur atom for S-doped case in the supercell. As the K concentration is high, four K atoms are introduced in the layers, which corresponds to one K atom per primitive cell. For the K, S-co-doped CN, one N is replaced by one S and four K atoms are introduced, which gives the ratio of S to K 1:4. Although this is higher than the experimental ratio, the local environment of the K, S situated position is suitable to study the effects from the doping on the reactions. The Gibbs free potential energy landscapes for the 2e-ORR reaction over pristine, S-doped, K-doped and K, S-co-doped CN are shown in Fig. 5a. In the first stage along the reaction coordinates, the reference state refers to each CN molecule with H₂ and O₂ in the gas phase with a pressure of 1 bar at room temperature. The behavior of oxygen adsorption varies among the four systems. The O₂ adsorption is endergonic for pristine (green) and S-doped (red) CN. After introducing K atoms in the system, the O₂ adsorption becomes exergonic for the K-doped and K, S co-doped cases. After the adsorption of O₂, the consequent hydrogenation steps involving OOH* and H₂O₂* formation can proceed as exergonic processes compared with the reference level for all systems. For K-doped and K, S co-doped CN, the desorption of H₂O₂* to the liquid phase is endergonic and is considered as the rate-limiting step. Additionally, the effect from OH groups have been investigated by constructing two CN fragments with different sizes. The potential energy surface shows that O₂ adsorption becomes unfavorable with the adsorption site in close proximity to the -OH termination. With the adsorption site further away from the -OH termination, the O₂ adsorption becomes feasible with a similar adsorption energy compared to the CN structure without -OH group terminations (Fig. S18a). Compared with the structure of CNKS in Fig. S18b, the structure of CNKS-OH in Fig. S18c and S18d show that the O₂ adsorption site is nearby the -OH terminations and the O₂ adsorption site is further away from the -OH terminations, respectively. Though the adsorption becomes unfeasible on the sites close to OH terminations at the edges, there are still abundant sites further away from the edge, which can give the ORR reaction activity. Therefore, we do not think the -OH terminations can have dramatic effects on the ORR reaction activity. To understand the difference in O₂ adsorption among the four considered systems, the charge density prior to and after the adsorption of O₂ step is analyzed for each system, and the difference is presented in Fig. 5b. It can be seen that the electron redistribution upon the adsorption on the pristine CN is negligible compared to the other three systems. Although there is a significant amount of electron accumulation in the π orbital of O₂ for the adsorption on S-doped CN, the electron depletion between the C–O bond is smaller compared with the K-doped and K, S co-doped systems, implying less electron transfer for the S-doped case. Moreover, the bond length of adsorbed O₂ is 1.24 Å for pristine CN and 1.30 Å for the S-doped case (compared to 1.23 Å in the gas phase), respectively, which implies that the adsorbed O₂ is still inactive. The bond length of the adsorbed O₂ increases to 1.38 for K-doped case and 1.40 Å for K, S co-doped CN, indicating that the adsorbed O₂ turns into a superoxide anion. The structural models for each system are provided in Fig. 5c. Furthermore, the bader charge analysis (see the red color in Fig. 5d) confirms the hypothesis of the superoxide anion with the charge value of –0.84 |e| for the adsorbed O₂ on K, S-co-doped CN. The charge value for the adsorbed O₂ decreases linearly from nearly zero for the pristine CN to nearly –0.8 |e| for K-doped CN. The Zero-Point-Energy (ZPE) corrected adsorption energies of O₂ over the four systems (see blue color in Fig. 5d) show the linear dependency of the adsorption energy with respect to the charge value of the O₂^{*}. To sum up, the K, S-co-doped CN exhibits remarkable capabilities in generating •O₂⁻, which could greatly contribute to the process of glucose photo-oxidation, ultimately leading to the production of gluconic acid.

Based on the experimental and theoretical results, a detailed mechanism of cellobiose photoreforming into gluconic acid with syngas co-production is then proposed (Fig. 5e). Firstly, the oxygen atom of cellobiose that bonds two glucose units reacts with acidic proton to form the corresponding conjugated acid (intermediate I) under acidic

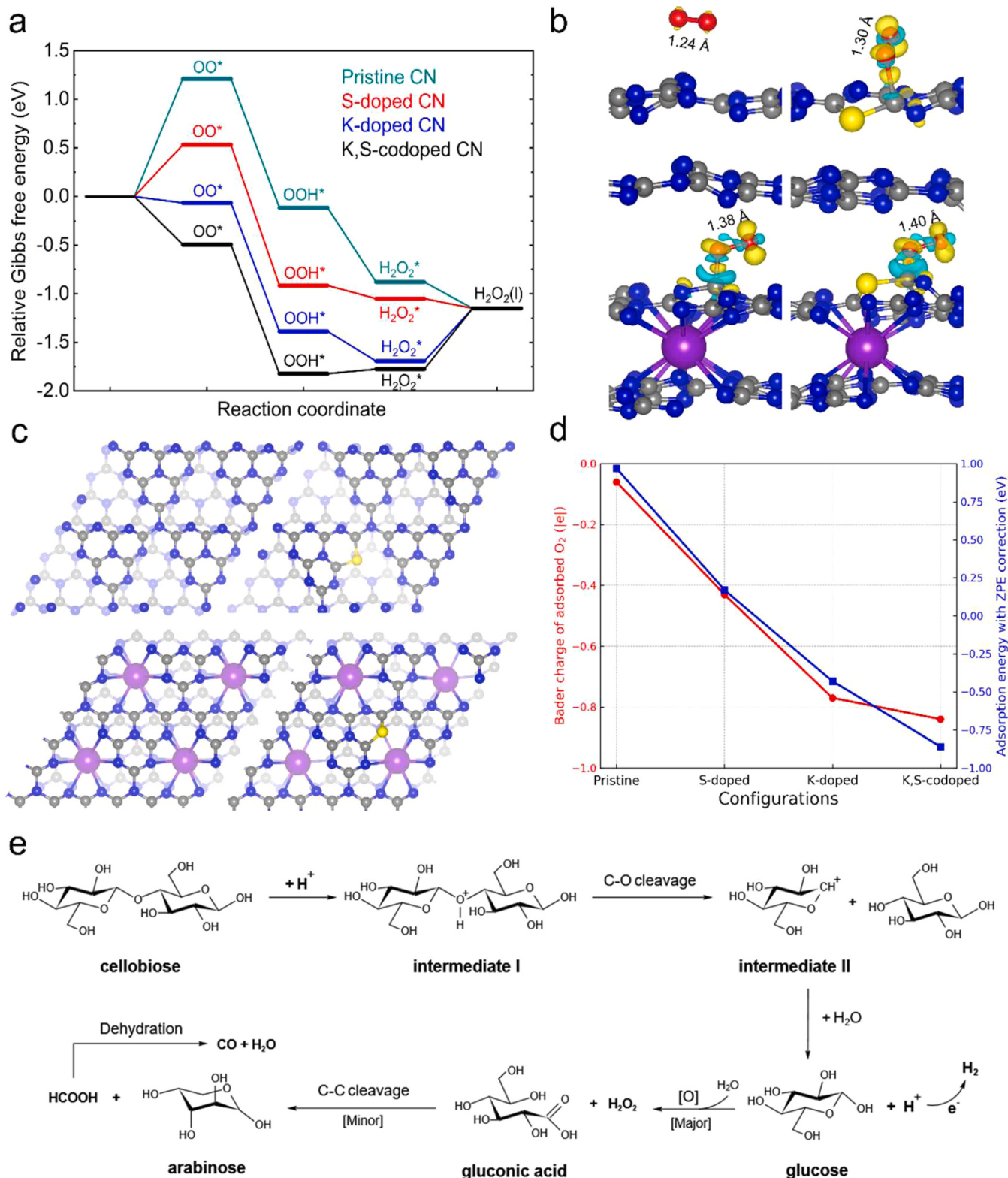


Fig. 5. (a) Potential Gibbs free energy landscape over K, S-co-doped CN system (black line). For comparison, the reactions are also calculated for pristine (green), S-doped (red) and K-doped (blue) CN systems, respectively. (b) Charge density difference $\Delta\rho(r)$ for adsorbed O_2 over each system. Blue and yellow contours represent regions of electron depletion and accumulation, respectively (isovalue of ± 0.01 electron Å^{-3}). The bond length of adsorbed O_2 is also indicated for each case. (c) Top view of the investigated structural model for each system. The atoms in the bottom layer are dimmer to facilitate visualization. (d) Bader charge of the adsorbed O_2 is plotted for each system (red color) and the Zero-Point-Energy (ZPE) corrected adsorption energy of O_2 is also shown for each system (blue color). Atom color codes: C (grey), N (blue), O (red), S (yellow) and K (purple). (e) Proposed mechanism of cellobiose photoreforming for gluconic acid and syngas production.

condition [57]. The cleavage of β -1,4-glycosidic bond, namely C-O bond, and breakdown of the conjugated acid then occurs, forming the cyclic carbonium ion (intermediate II) through a half-chair conformation, followed by the release of glucose and a proton after rapid addition of H_2O [57–59]. The formation of H_2 is most likely derived from the reduction of protons in acidic solution by photogenerated electrons. Then gluconic acid is obtained under the effect of major reactive oxidative species ($\bullet\text{O}_2^-$) with concomitant H_2O_2 formation. Typically, $\bullet\text{O}_2^-$ could deprotonate glucose, resulting in the formation of gluconolactone, then combine with electron to generate H_2O_2 , and gluconolactone subsequently undergoes spontaneous hydrolysis to yield gluconic acid [33,60]. Then gluconic acid could be partially decomposed into arabinose and formic acid by decarboxylation process via C1-C2 α -scissions [47,61]. Formic acid could be subsequently converted to generate CO through dehydration process [62]. Herein, the current work showcases significant capacity of a bifunctional photocatalyst towards the cellobiose photoreforming into simultaneous gluconic acid and syngas production.

4. Conclusions

In summary, a bifunctional CN photocatalyst with co-doping of potassium and sulfur has been successfully synthesized in this study. The rationally-designed carbon nitride not only realizes improved absorption of visible light and excellent charge separation efficiency, but also realizes selective gluconic acid production by the superior performance of the generation of $\bullet\text{O}_2^-$, which is demonstrated by DFT calculations. Additionally, cellobiose is not only more efficiently hydrolyzed into glucose but also promotes the syngas and gluconic acid production under acidic conditions. Consequently, the finely designed potassium/sulfur co-doped CN exhibited $> 80\%$ cellobiose conversion and $> 70\%$ gluconic acid selectivity coupled with syngas production ($\sim 56 \mu\text{mol g}^{-1} \text{h}^{-1}$) in acidic conditions under light illumination. The present work shews new light to design a bifunctional photocatalyst for the simultaneous production of gluconic acid and syngas from cellobiose photoreforming.

CRediT authorship contribution statement

Jiu Wang: Investigation, Methodology, Writing – original draft, Writing – review & editing. **Heng Zhao:** Investigation, Methodology, Writing – review & editing. **Lin Chen:** Writing – review & editing, DFT calculations. **Jonas Björk:** DFT calculations. **Johanna Rosen:** DFT calculations. **Pawan Kumar:** Investigation, Methodology. **Liquan Jing:** Investigation, Methodology. **Jun Chen:** Investigation, Methodology. **Md Golam Kibria:** Supervision, Validation, Writing – review & editing. **Jinguang Hu:** Project administration, Supervision, Validation, Writing – review & editing, Funding acquisition. All authors discussed the results and commented on the manuscript.

Declaration of Competing Interest

The authors declare that they have no known competing financial interests or personal relationships that could have appeared to influence the work reported in this paper.

Data Availability

Data will be made available on request.

Acknowledgements

The authors acknowledge funding from the Canada First Research Excellence Fund (CFREF) and the Göran Gustafsson Foundation for Research in Natural Sciences and Medicine. The computations were enabled by resources provided by the National Academic Infrastructure

for Supercomputing in Sweden (NAIIS), funded by the Swedish Research Council through grant agreements no. 2022–06725 and no. 2018–05973.

Appendix A. Supporting information

Supplementary data associated with this article can be found in the online version at doi:10.1016/j.apcatb.2023.123665.

References

- [1] B. Song, R. Lin, C.H. Lam, H. Wu, T.-H. Tsui, Y. Yu, Recent advances and challenges of inter-disciplinary biomass valorization by integrating hydrothermal and biological techniques, *Renew. Sustain. Energy Rev.* 135 (2021), 110370.
- [2] E. Daneshvar, R.J. Wicker, P.-L. Show, A. Bhatnagar, Biologically-mediated carbon capture and utilization by microalgae towards sustainable CO_2 biofixation and biomass valorization—a review, *Chem. Eng. J.* 427 (2022), 130884.
- [3] X. Wu, N. Luo, S. Xie, H. Zhang, Q. Zhang, F. Wang, Y. Wang, Photocatalytic transformations of lignocellulosic biomass into chemicals, *Chem. Soc. Rev.* 49 (2020) 6198–6223.
- [4] J. Wang, H. Shirvani, H. Zhao, M.G. Kibria, J. Hu, Lignocellulosic biomass valorization via bio-photo/electro hybrid catalytic systems, *Biotechnol. Adv.* 66 (2023), 108157.
- [5] J. Wang, H. Zhao, B. Zhu, S. Larter, S. Cao, J. Yu, M.G. Kibria, J. Hu, Solar-driven glucose isomerization into fructose via transient lewis acid–base active sites, *ACS Catal.* 11 (2021) 12170–12178.
- [6] X. Bai, Q. Hou, H. Qian, Y. Nie, T. Xia, R. Lai, G. Yu, M.L.U. Rehman, H. Xie, M. Ju, Selective oxidation of glucose to gluconic acid and glucaric acid with chlorin e6 modified carbon nitride as metal-free photocatalyst, *Appl. Catal. B* 303 (2022), 120895.
- [7] J. Wang, X. Wang, H. Zhao, J.F. Van Humbeck, B.N. Richtik, M.R. Dolgos, A. Seifitokaldani, M.G. Kibria, J. Hu, Selective C3–C4 cleavage via glucose photoreforming under the effect of nucleophilic dimethyl sulfoxide, *ACS Catal.* 12 (2022) 14418–14428.
- [8] H. Zhao, X. Yu, C.-F. Li, W. Yu, A. Wang, Z.-Y. Hu, S. Larter, Y. Li, M.G. Kibria, J. Hu, Carbon quantum dots modified TiO_2 composites for hydrogen production and selective glucose photoreforming, *J. Energy Chem.* 64 (2022) 201–208.
- [9] S. Carlier, S. Hermans, Highly efficient and recyclable catalysts for cellobiose hydrolysis: systematic comparison of carbon nanomaterials functionalized with benzyl sulfonic acids, *Front. Chem.* 8 (2020) 347.
- [10] H. Zhao, C.-F. Li, X. Yu, N. Zhong, Z.-Y. Hu, Y. Li, S. Larter, M.G. Kibria, J. Hu, Mechanistic understanding of cellulose β -1, 4-glycosidic cleavage via photocatalysis, *Appl. Catal. B* 302 (2022), 120872.
- [11] R. Rinaldi, F. Schütt, Acid hydrolysis of cellulose as the entry point into biorefinery schemes, *ChemSusChem* 2 (2009) 1096–1107.
- [12] S. Van de Vyver, J. Geboers, P.A. Jacobs, B.F. Sels, Recent advances in the catalytic conversion of cellulose, *ChemCatChem* 3 (2011) 82–94.
- [13] K.-i Shimizu, H. Furukawa, N. Kobayashi, Y. Itaya, A. Satsuma, Effects of Brønsted and Lewis acidities on activity and selectivity of heteropolyacid-based catalysts for hydrolysis of cellobiose and cellulose, *Green. Chem.* 11 (2009) 1627–1632.
- [14] S. Cao, J. Low, J. Yu, M. Jaroniec, Polymeric photocatalysts based on graphitic carbon nitride, *Adv. Mater.* 27 (2015) 2150–2176.
- [15] S. Cao, H. Li, T. Tong, H.C. Chen, A. Yu, J. Yu, H.M. Chen, Single-atom engineering of directional charge transfer channels and active sites for photocatalytic hydrogen evolution, *Adv. Funct. Mater.* 28 (2018) 1802169.
- [16] J. Jiang, D. Duan, J. Ma, Y. Jiang, R. Long, C. Gao, Y. Xiong, Van der waals heterostructures by single cobalt sites-anchored graphene and g-C3N4 nanosheets for photocatalytic syngas production with tunable CO/H_2 ratio, *Appl. Catal. B* 295 (2021), 120261.
- [17] J. Ma, Y. Li, D. Jin, X. Yang, G. Jiao, K. Liu, S. Sun, J. Zhou, R. Sun, Reasonable regulation of carbon/nitride ratio in carbon nitride for efficient photocatalytic reforming of biomass-derived feedstocks to lactic acid, *Appl. Catal. B* 299 (2021), 120698.
- [18] H. Zhao, X. Wang, X. Wu, J. Wang, N. Zhong, A. Seifitokaldani, S. Larter, M. G. Kibria, J. Hu, Exploration of optimal reaction conditions on lactic acid production from glucose photoreforming over carbon nitride, *Resour. Chem. Mater.* 2 (2023) 111–116.
- [19] H. Zhang, H. Zhao, S. Zhai, R. Zhao, J. Wang, X. Cheng, H.S. Shiran, S. Larter, M. G. Kibria, J. Hu, Electron-enriched Lewis acid-base sites on red carbon nitride for simultaneous hydrogen production and glucose isomerization, *Appl. Catal. B* 316 (2022), 121647.
- [20] J. Wang, S. Cao, J. Yu, Nanocages of polymeric carbon nitride from low-temperature supramolecular preorganization for photocatalytic CO_2 reduction, *Sol. RRI* 4 (2020) 1900469.
- [21] J. Ma, D. Jin, X. Yang, S. Sun, J. Zhou, R. Sun, Phosphorus-doped carbon nitride with grafted sulfonic acid groups for efficient photocatalytic synthesis of xylonic acid, *Green. Chem.* 23 (2021) 4150–4160.
- [22] G. Kresse, J. Hafner, Ab initio molecular dynamics for open-shell transition metals, *Phys. Rev. B* 48 (1993) 13115.
- [23] G. Kresse, J. Hafner, Ab initio molecular-dynamics simulation of the liquid–metal–amorphous–semiconductor transition in germanium, *Phys. Rev. B* 49 (1994) 14251.

[24] G. Kresse, J. Furthmüller, Efficient iterative schemes for ab initio total-energy calculations using a plane-wave basis set, *Phys. Rev. B* 54 (1996) 11169.

[25] P.E. Blöchl, Projector augmented-wave method, *Phys. Rev. B* 50 (1994) 17953.

[26] G. Kresse, D. Joubert, From ultrasoft pseudopotentials to the projector augmented-wave method, *Phys. Rev. B* 59 (1999) 1758.

[27] I. Hamada, van der Waals density functional made accurate, *Phys. Rev. B* 89 (2014), 121103.

[28] H.-J. Kim, S.-H. Kang, I. Hamada, Y.-W. Son, Origins of the structural phase transitions in MoTe_2 and WTe_2 , *Phys. Rev. B* 95 (2017), 180101.

[29] K. Momma, F. Izumi, VESTA 3 for three-dimensional visualization of crystal, volumetric and morphological data, *J. Appl. Crystallogr.* 44 (2011) 1272–1276.

[30] G. Henkelman, A. Arnaldsson, H. Jónsson, A fast and robust algorithm for Bader decomposition of charge density, *Comp. Mater. Sci.* 36 (2006) 354–360.

[31] W. Tang, E. Sanville, G. Henkelman, A grid-based Bader analysis algorithm without lattice bias, *J. Phys.: Condens. Matter* 21 (2009), 084204.

[32] H. Yu, R. Shi, Y. Zhao, T. Bian, Y. Zhao, C. Zhou, G.I. Waterhouse, L.Z. Wu, C. H. Tung, T. Zhang, Alkali-assisted synthesis of nitrogen deficient graphitic carbon nitride with tunable band structures for efficient visible-light-driven hydrogen evolution, *Adv. Mater.* 29 (2017) 1605148.

[33] P. Zhang, D. Sun, A. Cho, S. Weon, S. Lee, J. Lee, J.W. Han, D.-P. Kim, W. Choi, Modified carbon nitride nanzyme as bifunctional glucose oxidase-peroxidase for metal-free bioinspired cascade photocatalysis, *Nat. Commun.* 10 (2019) 1–14.

[34] G. Zhang, G. Li, T. Heil, S. Zafeiratos, F. Lai, A. Savateev, M. Antonietti, X. Wang, Tailoring the grain boundary chemistry of polymeric carbon nitride for enhanced solar hydrogen production and CO_2 reduction, *Angew. Chem. Int. Ed.* 58 (2019) 3433–3437.

[35] P. Zhang, Y. Tong, Y. Liu, J.J.M. Vequizo, H. Sun, C. Yang, A. Yamakata, F. Fan, W. Lin, X. Wang, W. Choi, Heteroatom dopants promote two-electron O_2 reduction for photocatalytic production of H_2O_2 on polymeric carbon nitride, *Angew. Chem. Int. Ed.* 59 (2020) 16209–16217.

[36] Y. Yang, S. Wang, Y. Jiao, Z. Wang, M. Xiao, A. Du, Y. Li, J. Wang, L. Wang, An unusual red carbon nitride to boost the photoelectrochemical performance of wide bandgap photoanodes, *Adv. Funct. Mater.* 28 (2018) 1805698.

[37] B. Luo, R. Song, J. Geng, X. Liu, D. Jing, M. Wang, C. Cheng, Towards the prominent cocatalytic effect of ultra-small CoP particles anchored on g-C₃N₄ nanosheets for visible light driven photocatalytic H_2 production, *Appl. Catal. B* 256 (2019), 117819.

[38] H. Li, B. Zhu, S. Cao, J. Yu, Controlling defects in crystalline carbon nitride to optimize photocatalytic CO_2 reduction, *Chem. Commun.* 56 (2020) 5641–5644.

[39] J. Liu, W. Fang, Z. Wei, Z. Qin, Z. Jiang, W. Shangguan, Efficient photocatalytic hydrogen evolution on N-deficient g-C₃N₄ achieved by a molten salt post-treatment approach, *Appl. Catal. B* 238 (2018) 465–470.

[40] Z. Jiang, W. Wan, H. Li, S. Yuan, H. Zhao, P.K. Wong, A hierarchical Z-scheme $\alpha\text{-Fe}_2\text{O}_3/\text{g-C}_3\text{N}_4$ hybrid for enhanced photocatalytic CO_2 reduction, *Adv. Mater.* 30 (2018) 1706108.

[41] P. Chen, X. Dong, M. Huang, K. Li, L. Xiao, J. Sheng, S. Chen, Y. Zhou, F. Dong, Rapid self-decomposition of g-C₃N₄ during gas-solid photocatalytic CO_2 reduction and its effects on performance assessment, *ACS Catal.* 12 (2022) 4560–4570.

[42] Y. Guo, T. Chen, Q. Liu, Z. Zhang, X. Fang, Insight into the enhanced photocatalytic activity of potassium and iodine codoped graphitic carbon nitride photocatalysts, *J. Phys. Chem. C* 120 (2016) 25328–25337.

[43] C. Hu, W.-Z. Hung, M.-S. Wang, P.-J. Lu, Phosphorus and sulfur codoped g-C₃N₄ as an efficient metal-free photocatalyst, *Carbon* 127 (2018) 374–383.

[44] Y. Hu, Y. Shim, J. Oh, S. Park, S. Park, Y. Ishii, Synthesis of ¹³C-, ¹⁵N-labeled graphitic carbon nitrides and NMR-based evidence of hydrogen-bonding assisted two-dimensional assembly, *Chem. Mater.* 29 (2017) 5080–5089.

[45] V.W.-h Lau, I. Moudrakovski, T. Botari, S. Weinberger, M.B. Mesch, V. Duppel, J. Senker, V. Blum, B.V. Lotsch, Rational design of carbon nitride photocatalysts by identification of cyanamide defects as catalytically relevant sites, *Nat. Commun.* 7 (1) (2016) 10.

[46] F.-Y. Su, C.-Q. Xu, Y.-X. Yu, W.-D. Zhang, Carbon self-doping induced activation of n-π* electronic transitions of g-C₃N₄ nanosheets for efficient photocatalytic H_2 evolution, *ChemCatChem* 8 (2016) 3527–3535.

[47] H. Zhao, P. Liu, X. Wu, A. Wang, D. Zheng, S. Wang, Z. Chen, S. Larter, Y. Li, B.-L. Su, M.G. Kibria, J. Hu, Plasmon enhanced glucose photoreforming for arabinose and gas fuel co-production over 3DOM TiO₂-Au, *Appl. Catal. B* 291 (2021), 120055.

[48] Q. Zhang, Z. Wan, K. Iris, D.C. Tsang, Sustainable production of high-value gluconic acid and glucaric acid through oxidation of biomass-derived glucose: a critical review, *J. Clean. Prod.* 312 (2021), 127745.

[49] J. Wang, L. Chen, H. Zhao, P. Kumar, S.R. Larter, M.G. Kibria, J. Hu, In situ photo-fenton-like tandem reaction for selective gluconic acid production from glucose photo-oxidation, *ACS Catal.* 13 (2023) 2637–2646.

[50] Z. Eroglu, O. Metin, Internal interactions within the complex Type-II heterojunction of a graphitic carbon nitride/black phosphorus hybrid decorated with graphene quantum dots: implications for photooxidation performance, *ACS Appl. Nano Mater.* 6 (2023) 7960–7974.

[51] M. Shalom, S. Inal, C. Fettkenhauer, D. Neher, M. Antonietti, Improving carbon nitride photocatalysis by supramolecular preorganization of monomers, *J. Am. Chem. Soc.* 135 (2013) 7118–7121.

[52] Z. Chen, A. Savateev, S. Pronkin, V. Papaefthimiou, C. Wolff, M.G. Willinger, E. Willinger, D. Neher, M. Antonietti, D. Dontsova, "The Easier the Better" preparation of efficient photocatalysts—metastable poly (heptazine imide) salts, *Adv. Mater.* 29 (2017) 1700555.

[53] F. He, B. Zhu, B. Cheng, J. Yu, W. Ho, W. Macyk, 2D/2D/0D TiO₂/C₃N₄/Ti₃C₂ MXene composite S-scheme photocatalyst with enhanced CO_2 reduction activity, *Appl. Catal. B* 272 (2020), 119006.

[54] X. Zeng, Y. Liu, X. Hu, X. Zhang, Photoredox catalysis over semiconductors for light-driven hydrogen peroxide production, *Green. Chem.* 23 (2021) 1466–1494.

[55] J. Wang, D. Hao, J. Ye, N. Umezawa, Determination of crystal structure of graphitic carbon nitride: ab initio evolutionary search and experimental validation, *Chem. Mater.* 29 (2017) 2694–2707.

[56] T. Xiong, W. Cen, Y. Zhang, F. Dong, Bridging the g-C₃N₄ interlayers for enhanced photocatalysis, *ACS Catal.* 6 (2016) 2462–2472.

[57] S. Sasmal, K. Mohanty, Pretreatment of lignocellulosic biomass toward biofuel production, *Bioref. Biomass Biofuels: Oppor. Percept.* (2018) 203–221.

[58] L. Peña, M. Ikenberry, B. Ware, K.L. Hohn, D. Boyle, X.S. Sun, D. Wang, Cellulose hydrolysis using acid-functionalized nanoparticles, *Biotechnol. Bioprocess Eng.* 16 (2011) 1214–1222.

[59] S.J. Dee, A.T. Bell, A study of the acid-catalyzed hydrolysis of cellulose dissolved in ionic liquids and the factors influencing the dehydration of glucose and the formation of humins, *ChemSusChem* 4 (2011) 1166–1173.

[60] J. Wang, H. Zhao, S. Larter, M.G. Kibria, J. Hu, One-pot sequential cascade reaction for selective gluconic acid production from cellulose photobiorefining, *Chem. Commun.* 59 (2023) 3451–3454.

[61] J. Wang, H. Zhao, P. Liu, N. Yasri, N. Zhong, M.G. Kibria, J. Hu, Selective superoxide radical generation for glucose photoreforming into arabinose, *J. Energy Chem.* 74 (2022) 324–331.

[62] M.F. Kuehnel, D.W. Wakerley, K.L. Orchard, E. Reisner, Photocatalytic formic acid conversion on CdS nanocrystals with controllable selectivity for H_2 or CO , *Angew. Chem. Int. Ed.* 54 (2015) 9627–9631.